

Chapter 2

Trapped-Ion Qubits

In this chapter we give an overview of how one can use a calcium ion as a qubit. We then review the operation of a Paul trap, and discuss the quantised behaviour of a ‘crystal’ of trapped ions near their motional ground state. The shared motional degrees of freedom of such a crystal allow the implementation of quantum ‘logic gates’, i.e. multi-qubit entangling operations.

2.1 The Calcium Ion as a Qubit

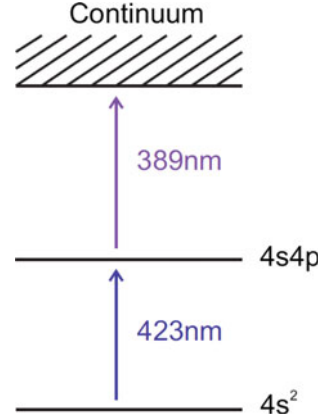
In this work we use two different isotopes of singly-ionised calcium as qubits, $^{43}\text{Ca}^+$ (nuclear spin $I = 7/2$) and $^{40}\text{Ca}^+$ ($I = 0$). In the following we describe the atomic structure of the calcium ion, how we create and Doppler-cool the ions, and how we initialise, manipulate, and read out the quantum state of the ion.

2.1.1 Photo-Ionisation

Before we do anything we have to create calcium ions. This can be done by brute force – bombarding a calcium atom with energetic electrons until a valence electron is knocked off the atom – but this can ionize any species effusing from the calcium source (a resistively heated oven). Instead, we use a much more elegant scheme that is not just atomic species selective, but isotope selective (Fig. 2.1). This scheme is two-step photo-ionisation [LRH+04, GRB+01].

In this scheme we use two lasers. The first laser is resonant with the $4s^2$ - $4s4p$ transition in neutral calcium (423 nm, line-width ~ 35 MHz). As the isotope shifts in this transition are ~ 1 GHz (larger than the line-width, provided that a Doppler-free geometry is used) only one isotope is excited to the $4s4p$ level. The second laser

Fig. 2.1 Energy level diagram for neutral calcium showing the transitions relevant to the photo-ionisation process



(389 nm) provides enough energy to excite from the $4s4p$ level to the continuum, but not enough to reach the continuum from the ground state. This isotope selectivity is very useful, as it means we can selectively load one of the several isotopes of calcium in our oven, simply by adjusting the frequency of the 423 nm laser.

2.1.2 Doppler Cooling

To detect the presence of the ions, and to cool their motion, we scatter photons off the ions, and detect the scattered photons with an imaging system. To scatter photons we excite the $4S_{1/2} - 4P_{1/2}$ (397 nm) transition with a laser. From this near-cycling transition there is a $\sim 5\%$ probability of decay to the $3D_{3/2}$ state (Fig. 2.2). We repump this lost population by driving the $3D_{3/2} - 4P_{1/2}$ (866 nm) transition.

In an isotope without nuclear spin (e.g. $^{40}\text{Ca}^+$) this can be efficiently done with monochromatic radiation. In $^{43}\text{Ca}^+$ ($I = 7/2$) this requires two frequencies of 397 nm light to repump the ≈ 3.2 GHz $S_{1/2}$ hyperfine splitting, and is somewhat less efficient [Szw09, Har13, Jan14].

2.1.3 The Qubit and Coherent Manipulations

We want the two qubit states ($|0\rangle$ and $|1\rangle$) to be as similar in nature as possible, so that environmental perturbations do not cause a differential energy shift of the qubit (leading to decoherence). We also need to be able to prepare into one of the qubit states to initialise the qubit, and be able to read out the qubit state precisely in a single-shot.

The qubits we use in this thesis all consist of two states in the ground level $4S_{1/2}$. These states do not spontaneously decay (if we prepare an atom in one of the ground states, it will stay in that state indefinitely), but do lose their phase coherence due to magnetic field noise. In $^{40}\text{Ca}^+$ there are only two ground states, so we do not have a

Fig. 2.2 Energy level diagram for the *low* lying levels of Ca^+ . The wavelengths and branching ratios of the dipole-allowed transitions are shown. The hyperfine splitting in $^{43}\text{Ca}^+$ is shown for the $4\text{S}_{1/2}$ level only. The precise transition frequencies and decay rates are given in Appendix A

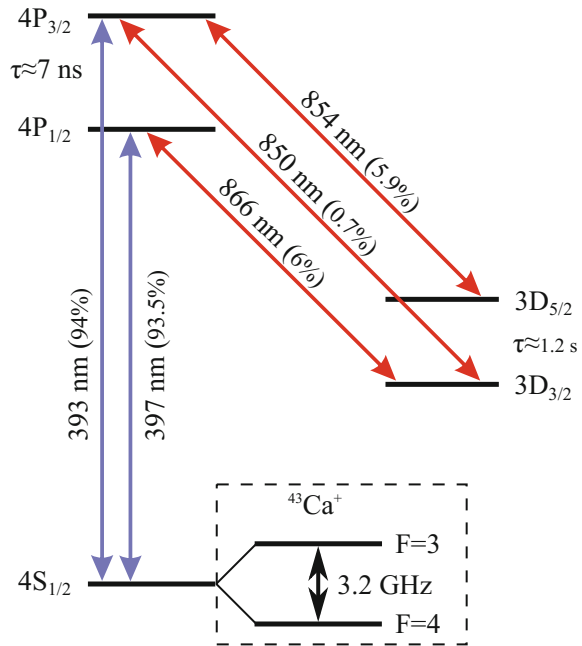
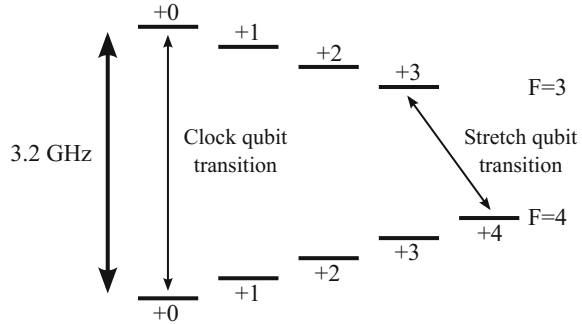


Fig. 2.3 The $4\text{S}_{1/2}$ ground level of $^{43}\text{Ca}^+$, with the two qubits we use labelled



choice of qubit. In $^{43}\text{Ca}^+$ there are 16 ground states, leading to many potential qubits (Fig. 2.3). The two we commonly use are the ‘stretch’ qubit ($\text{S}_{1/2}^{4,+4} - \text{S}_{1/2}^{3,+3}$) and the ‘low-field clock’ qubit ($\text{S}_{1/2}^{4,0} - \text{S}_{1/2}^{3,0}$).

The stretch qubit can be prepared and read out with high fidelity by optical pumping, but is highly magnetically sensitive (2.45 kHz/mG), whereas the clock qubit is harder to prepare and read out, but much less magnetically sensitive (4.8 Hz/mG for $B_0 = 2\text{G}$).¹

¹The clock qubit is first order insensitive to magnetic field variation at zero magnetic field, but we need to apply a quantisation field of $\sim 2\text{G}$ in order to read out and prepare the qubit efficiently, giving rise to a small first-order dependence.

We manipulate the state of these qubits in two ways. We directly drive the qubit transition using radiation in the RF to microwave regime, or we drive the qubit via a third level using the stimulated Raman effect. As we see in Chap. 3 there are several advantages (and disadvantages) to using the Raman effect over directly driving the qubit transition.

We can describe either of these manipulations as a pseudo-spin coupling. Our interaction Hamiltonian is

$$\begin{aligned} H_I &= -\boldsymbol{\mu} \cdot \mathbf{B} \\ \boldsymbol{\mu} &= \mu_m \mathbf{S} \\ \mathbf{B} &= B \hat{\mathbf{x}} \cos(\mathbf{k} \cdot \mathbf{r} - \omega t + \phi) \end{aligned} \quad (2.1)$$

where $\boldsymbol{\mu}$ is our pseudo-spin, \mathbf{r} the position of the ion, and \mathbf{k}, ω, ϕ the wave-vector, frequency, and phase of the applied (travelling-wave) radiation. The pseudo-spin basis is our two qubit states $\{|\uparrow\rangle, |\downarrow\rangle\}$. Moving into the interaction picture with respect to the spin ($H_0 = \frac{1}{2}\omega_0\sigma_z$) and dropping far off-resonant terms,

$$H_I = \frac{\Omega}{2} \sigma_+ \exp(i\mathbf{k} \cdot \mathbf{r} - i\delta t + i\phi) + \text{h.c.} \quad (2.2)$$

where $\delta := \omega - \omega_0$, and $\Omega = -\mu_m B$ is our Rabi frequency.

2.1.4 Readout of the Qubit State

After we have manipulated the qubit we want to read-out the result, i.e. detect the state of a single atom – this is generally a hard thing to do. However the technique of ‘electron shelving’ [Deh75] allows us to amplify this small difference in atomic state into a very large difference in fluorescence rate, and hence detect the state accurately.

The $3D_{5/2}$ level is long-lived ($\tau \approx 1.2$ s) and outside the Doppler cooling cycle ($4S_{1/2} - 4P_{1/2} - 3D_{3/2}$): if the ion is in $3D_{5/2}$ it will not scatter any 397 nm photons. By counting the photons scattered by the ion we can quickly detect, with high fidelity, if the ion is in the $4S_{1/2}$ state or the $3D_{5/2}$ state [MSW+08, Bur10].

We now need a way of mapping one of our $4S_{1/2}$ qubit states to $3D_{5/2}$ while not affecting the other. The technique we use for $^{40}\text{Ca}^+$ involves using a weak σ^+ polarised 393 nm beam and an intense σ^- polarised 850 nm beam [MSW+04]. With these beams there is a two-photon resonance for one of the qubit states that suppresses population transfer out of $4S_{1/2}$ while the other qubit state is freely pumped out of $4S_{1/2}$ to $3D_{5/2}$ ($\sim 90\%$) and $3D_{3/2}$ ($\sim 10\%$). The favourable branching ratios into the $3D_{5/2}$ shelf leads to a maximum shelving fidelity of 90%, hence a minimum *average* readout error of $\bar{\epsilon} = \frac{1}{2}(\epsilon_D + \epsilon_S) = 5\%$.

In $^{43}\text{Ca}^+$ we implement a simpler and more robust scheme [MSW+08, Szw09]. We assume that one of the states we want to readout out is $4S_{1/2}^{4,+4}$, and that the other

is $4S_{1/2}^{3,*}$. A σ^+ polarised 393 nm beam tuned to the $4S_{1/2}^4 \leftrightarrow 4P_{3/2}^5$ transition (22 MHz linewidth) excites the population in $4S_{1/2}^{4,+4}$ to $4P_{3/2}^{5,+5}$, but does not excite population out of $S_{1/2}^3$ due to the ~ 3 GHz hyperfine splitting. The state $4P_{3/2}^{5,+5}$ can only decay to $3D_{5/2}$ (as desired), back to the qubit state the population started in ($4S_{1/2}^{4,+4}$), or to three well-defined states in $3D_{3/2}$. If we apply appropriately polarised repumping pulses on the 850 nm transition we can recover all the population out of $3D_{3/2}$, accurately mapping one of the qubit states to $3D_{5/2}$ while leaving the other qubit state in $4S_{1/2}$ with ultimate (theoretical) errors of $\approx 1 \times 10^{-4}$.

2.2 Linear Paul Traps

For the work in this thesis we want to confine a number of ions in a 3d harmonic trap – we don't care too much about the details of this confinement. A linear Paul trap performs this job admirably.

No static electric field arrangement can spatially confine in all three dimensions. If we expand the electric field about the centre of the trap and drop all but the first order terms we have

$$\frac{\mathbf{F}}{q} = \mathbf{E} = \alpha \mathbf{x} + \beta \mathbf{y} + \gamma \mathbf{z} \quad (2.3)$$

Poisson's equation ($\nabla \cdot \mathbf{E} = 0$) then dictates that $\alpha + \beta + \gamma = 0$, and thus that a static arrangement of electric fields can confine in at most two dimensions, and is anti-confining in the remaining direction(s).

A linear Paul trap generates its confining potential with an oscillating (RF) 2D quadrupole field in the radial plane and with a static quadrupole electric field in the axial dimension (z). The radial fields are generated by two pairs of 'blades' and the axial by a pair of 'end-caps'. In our apparatus one pair of these blades is connected to ground, and the other to an RF source with (zero-peak) voltage V_{RF} . The electric potentials generated by the RF voltage on the blades and the DC voltage on the endcaps are described, for small displacements from the trap centre, by

$$\begin{aligned} U_{\text{RF}} &= Q_x^{\text{RF}} x^2 - Q_y^{\text{RF}} y^2 + Q_z^{\text{RF}} z^2 & U_{\text{DC}} &= Q_z^{\text{DC}} \left[z^2 - \frac{1}{2}(x^2 + y^2) \right] \\ Q_x^{\text{RF}} &= \frac{\alpha_x V_{\text{RF}}}{\rho_0^2} & Q_y^{\text{RF}} &= \frac{\alpha_y V_{\text{RF}}}{\rho_0^2} \\ Q_z^{\text{RF}} &= \frac{\alpha_z V_{\text{RF}}}{2z_0^2} & Q_z^{\text{DC}} &= \frac{\alpha_z V_z}{z_0^2} \end{aligned} \quad (2.4)$$

where ρ_0 and z_0 are the blade-centre and endcap-centre spacings. The dimensionless parameters α characterise the geometry or 'efficiency' of the electrodes (hyperbolic infinitely-long RF electrodes have $\alpha_{x,y} = 1$).

Charged particles in the trap will feel, averaged over a period of the RF, a harmonic radial force. A derivation of this ponderomotive potential is outlined in [LL76]. When the Mathieu q parameter $q \ll 1$ the motion of a particle in the trap can be approximated as being the sum of secular motion and (small amplitude) micro-motion at the RF frequency. Substituting the trap potentials (Eq. 2.4) into the equation of motion and using the standard Mathieu equation approximations we find

$$\mathbf{q} = -\frac{4e}{m\Omega^2} \begin{pmatrix} Q_x^{\text{RF}} \\ -Q_y^{\text{RF}} \\ Q_z^{\text{RF}} \end{pmatrix} \quad \mathbf{a} = \frac{8e}{m\Omega^2} Q_z^{\text{DC}} \begin{pmatrix} -\frac{1}{2} \\ -\frac{1}{2} \\ 1 \end{pmatrix} \quad (2.5)$$

$$r_i \approx r_0 \cos(\omega_i t) \left(1 + \frac{q_i}{2} \cos \Omega t \right) \quad \omega_i = \frac{\Omega}{2} \sqrt{\frac{q_i^2}{2} + a_i} \quad (2.6)$$

where r_i is the approximate solution for small q , and ω_i is the secular frequency of the motion.

In general there is an axial RF potential gradient. This is due to the asymmetric driving of the blades. This can be understood by first considering a symmetrically driven trap, with one blade pair driven by RF with amplitude $+V_{\text{RF}}/2$, the other blade pair driven by RF with an amplitude $-V_{\text{RF}}/2$, and the end-caps at RF ground. In this case there is a line of zero potential along the axis of the trap. We now add an (oscillating) offset of $V_{\text{RF}}/2$ to all the electrodes. The blades are now at V_{RF} and 0, and the end-caps at $V_{\text{RF}}/2$. There is still no axial RF potential gradient. If we now hold the end-caps at RF ground we break the symmetry, and there is an axial RF potential gradient: the potential at the centre of the trap oscillates, but the potential from the end-caps is static. Thus for an asymmetrically driven trap there is an axial RF pseudo-potential, and more importantly, axial micro-motion.

2.2.1 Micro-Motion Detection and Compensation

Consider a static electric field displacing the ion from the RF potential null. The ion now sees an oscillating force, leading to periodic motion of the ion at the trap RF frequency – this is micro-motion. Excess micro-motion can also be caused by an RF phase difference between the driven trap blades, which leads to the RF null moving over the RF period [BMB+98]. In both cases the resulting micro-motion leads to Doppler broadening of or sidebands on the optical transitions, which can be undesirable.

We can detect micro-motion by correlating the ion fluorescence with the trap RF phase: the varying instantaneous velocity over the motional period gives rise to a varying Doppler shift. The amplitude of the correlation reveals the amplitude of the micro-motion projected onto the beam direction. By adding static electric fields to minimise the micro-motion seen in three linearly independent beam directions we can ensure the ion sits as close as possible to the RF potential null.

2.3 Motion of the Ions

In this section we discuss the quantized motion of a crystal of ions and introduce our notation.

We assume the (identical) ions are confined in a 3d harmonic trap with radial confinement much tighter than the axial. When sufficiently cold, the ions then form linear crystals along the axis. We define the weak axis as \hat{z} , and the two principle radial directions as \hat{x} , \hat{y} . The motion of the N ions can then be described by N normal modes in each of these three principal directions.

2.3.1 Quantization of Motion

We wish to find an expression for \mathbf{r}_n , the displacement of ion n from its equilibrium position. We do this by quantizing each of the normal modes of the motion, giving

$$\mathbf{r}_n = \sum_{\hat{q}=\hat{x},\hat{y},\hat{z}} \sum_{j=1}^N \hat{q} b_n^{(\hat{q},j)} \tilde{q}_{\hat{q},j} \left(a_{\hat{q},j} + a_{\hat{q},j}^\dagger \right) \quad (2.7)$$

where the first sum is over the principal axes, and the second is over the N normal modes in each direction. The normal mode matrix $b_n^{(\hat{q},j)}$ describes the amplitude of motion of ion n for the j 'th normal mode in the direction \hat{q} , normalised such that the $\sum_n \left(b_n^{(\hat{q},j)} \right)^2 = 1$ [Jam98]. The ground state wave-function size for each normal mode is given by $\tilde{q}_{\hat{q},j} = \sqrt{\hbar/(2m\omega_{\hat{q},j})}$.

For a single ion there is only one motional mode in each direction, the centre of mass (CoM) modes. For two ions the axial modes are the centre of mass mode $b^{(\hat{z},1)} = \frac{1}{\sqrt{2}}(1, 1)$ and the breathing mode $b^{(\hat{z},2)} = \frac{1}{\sqrt{2}}(1, -1)$. The radial modes are the centre of mass modes and the rocking modes (with the same normal mode coordinates).

2.3.2 Coupling to the Motion

For a general coupling between a spin and a travelling wave field (Eq. 2.2) the spatial dependence of the field leads to a coupling between spin and motion – we now consider the effect of this coupling. For simplicity we assume we only couple to the axial modes ($\mathbf{k} \propto \hat{z}$) and we write $b_n^{(\hat{z},j)} = b_n^{(j)}$. We quantize the motion and find the motion phase for ion n to be

$$\mathbf{k} \cdot \mathbf{r}_n = \mathbf{k} \cdot \hat{\mathbf{z}} \sum_j b_n^{(j)} \tilde{q}_j (a_j + a_j^\dagger) \quad (2.8)$$

$$= \sum_j \eta_n^{(j)} (a_j + a_j^\dagger) \quad (2.9)$$

where the Lamb–Dicke parameter, defined as

$$\eta_n^{(j)} = \mathbf{k} \cdot \hat{\mathbf{z}} \tilde{q}_j b_n^{(j)} \quad (2.10)$$

gives the coupling strength of the applied field to the motion of ion n and mode j . This depends on the angle between the coupling wave-vector and the mode direction ($\mathbf{k} \cdot \hat{\mathbf{z}}$), the motional mode frequency (via the spatial extent of the ground state wave packet, \tilde{q}), and the amplitude of motion of the ion for this particular mode ($b_n^{(j)}$).

We can now explicitly rewrite the motion phase factor from Eq. 2.2 in the interaction picture of $H_0 = \sum_j \omega_j (a_j^\dagger a_j + \frac{1}{2})$

$$\exp(i\mathbf{k} \cdot \mathbf{r}_m) = \sum_{\{n'\} \{n\}} |\{n'\}\rangle \langle \{n'\}| \prod_{j=1}^N \exp\left(i\eta_m^{(j)} (a_j + a_j^\dagger)\right) e^{i\omega_j(n'_j - n_j)t} |\{n\}\rangle \langle \{n\}| \quad (2.11)$$

where $\{n\}$ represents all of the combinations of n_1, n_2, \dots, n_N .

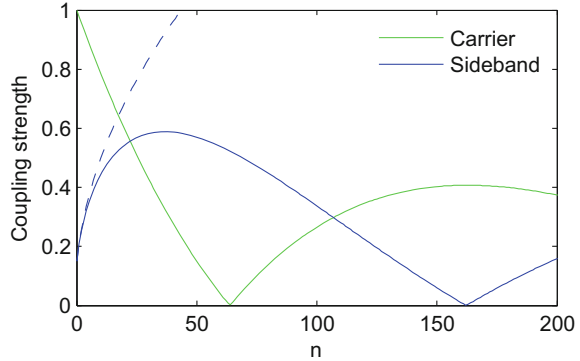
For one ion ($N = 1$) in the Lamb–Dicke regime ($\eta\sqrt{1 + 2n} \ll 1$) we can expand the coupling in a small angle approximation

$$\mathcal{H}_I = \frac{\Omega}{2} \sigma_+ (1 + i\eta(a^\dagger e^{i\omega_z t} + a e^{-i\omega_z t})) \exp(-i\delta t + i\phi) + \text{h.c.} \quad (2.12)$$

We can see that, assuming $\Omega \ll \omega_z$, we can tune to address the carrier ($\delta = 0$) and flip the spin without changing the motional state, or we can tune to the sidebands ($\delta = \pm\omega_z$) and add or subtract motional quanta while flipping the spin. In this limit the carrier Rabi frequency, Ω , is independent of motional state, and the sideband Rabi frequency is $\eta\Omega\sqrt{n}$. Outside the Lamb–Dicke regime these expressions break down. As n increases the motional wave-packet size becomes comparable to the wavelength of the driving field. This causes the amplitude of the driving field averaged over the wave-packet to decrease, giving a reduction in carrier Rabi frequency, as well as causing the gradient of the driving field over the wave-packet to decrease leading to a reduction in sideband Rabi frequency. This can be expressed analytically [WMI+98]

$$|\langle n' | \exp(i\eta(a + a^\dagger)) | n \rangle| = e^{-\eta^2/2} \sqrt{\frac{n_{<}!}{n_{>}!}} \eta^{|n' - n|} L_{n_{<}}^{|n' - n|}(\eta^2) \quad (2.13)$$

Fig. 2.4 Coupling strength to carrier and first motional sideband for $\eta = 0.15$. The *solid lines* show the full solution, and the *dashed lines* the solution in the Lamb–Dicke approximation



where $L_n^\alpha(x)$ is the generalised Laguerre polynomial, and $n_<$ ($n_>$) is the smaller (larger) of n and n' . This is plotted for a mode with $\eta = 0.15$ in Fig. 2.4. We see that the $\Delta n = 1$ matrix element deviates from the Lamb–Dicke regime expression \sqrt{n} , dropping to zero at $n \sim 160$.

References

- [LRH+04] Lucas, D.M., A. Ramos, J.P. Home, M.J. McDonnell, S. Nakayama, J.-P. Stacey, S.C. Webster, D.N. Stacey, and A.M. Steane. 2004. Isotope-selective photoionization for calcium ion trapping. *Physical Review A* 69 (1): 1–13.
- [GRB+01] Gulde, S., D. Rotter, P. Barton, F. Schmidt-Kaler, R. Blatt, and W. Hogervorst. 2001. Simple and efficient photo-ionization loading of ions for precision ion-trapping experiments. *Applied Physics B* 73 (8): 861–863.
- [Szw09] Szwerc, D.J. 2009. *High Fidelity Readout and Protection of a $^{43}\text{Ca}^+$ Trapped Ion Qubit*. PhD thesis, University of Oxford.
- [Har13] Harty, T.P. 2013. *High-Fidelity Microwave-Driven Quantum Logic in Intermediate-Field $^{43}\text{Ca}^+$* . PhD thesis.
- [Jan14] Janacek, H.A. 2014. *Simulating trapped-ion qubits using the optical Bloch equations*. PhD thesis, University of Oxford.
- [Deh75] Dehmelt, H. 1975. Proposed $10^{14} \delta\nu > \nu$ laser fluorescence spectroscopy of Ti^+ monocation oscillator II. *Bulletin of the American Physical Society* 20 (1): 60.
- [MSW+08] Myerson, A., D.J. Szwerc, S.C. Webster, D.T.C. Allcock, M.J. Curtis, G. Imreh, J.A. Sherman, D.N. Stacey, A.M. Steane, and D.M. Lucas. 2008. High-fidelity readout of trapped-ion qubits. *Physical Review Letters* 100 (20): 200502.
- [Bur10] Burrell, A.H. 2010. *High-fidelity readout of trapped-ion qubits*. PhD thesis, University of Oxford.
- [MSW+04] McDonnell, M.J., J.-P. Stacey, S.C. Webster, J.P. Home, A. Ramos, D.M. Lucas, D.N. Stacey, and A.M. Steane. 2004. High-efficiency detection of a single quantum of angular momentum by suppression of optical pumping. *Physical Review Letters* 93 (15): 1–4.
- [LL76] Landau, L.D. and E.M. Lifshitz. 1976. *Mechanics (3rd Ed.)*, pages 93–95. Butterworth-Heinemann.
- [BMB+98] Berkeland, D.J., J.D. Miller, J.C. Bergquist, W.M. Itano, and D.J. Wineland. Minimization of ion micromotion in a Paul trap. *Journal of Applied Physics*, 83(10), 1998.

- [Jam98] James, D.F.V. 1998. Quantum dynamics of cold trapped ions with application to quantum computation. *Applied Physics B: Lasers and Optics* 66 (2): 181–190.
- [WMI+98] Wineland, D.J., C. Monroe, W.M. Itano, D. Leibfried, B.E. King, and D.M. Meekhof. 1998. Experimental issues in coherent quantum-state manipulation of trapped atomic ions. *Journal Of Research Of The National Institute Of Standards And Technology*, 103(3).

High-Fidelity Quantum Logic in Ca^+
Ballance, C.J.

2017, XVI, 141 p. 80 illus., 30 illus. in color., Hardcover

ISBN: 978-3-319-68215-0